21st Australasian Fluid Mechanics Conference
Adelaide, Australia
10-13 December 2018

Simultaneous velocity and density measurements using PIV and PLIF in turbulent axisymmetric buoyant plumes

Himanshu Mishra and Jimmy Philip

Department of Mechanical Engineering
The University of Melbourne, Victoria 3010, Australia

Abstract

From violent volcanic eruptions to the rising clouds, turbulent plumes are omnipresent in nature at wide range of scales. The mixing and growth dynamics of a turbulent plume is important in fundamental understanding of turbulence as well as in modelling this complex fluid mechanics phenomenon. Closure of turbulence equation requires knowledge of fluxes, such as, $\langle w'b' \rangle$ (the averaged product of fluctuating vertical velocity and buoyancy). This necessitates simultaneous field measurements of velocity and density of the mixing fluids with high spatial and temporal resolution. Here, we present a methodology for obtaining simultaneous time resolved measurement of velocity and density in an axisymmetric turbulent plume using 2D-2C particle image velocimetry (PIV) and planar laser induced fluorescence (PLIF), respectively. The experiments are performed with refractive index matched fluids to remove uncertainties due to optical distortions. Based on the available literature [1], glycerine and mono-potassium phosphate (MPP) combination is used for refractive index matching. Attenuation coefficients due to glycerine and MPP are obtained for the first time and, it is found that this combination causes less attenuation of laser sheet compared to the commonly used mixture. Effect of PIV seeding particles, which is rarely considered in the literature is also estimated, and the attenuation due to these particles is found to be of the same order of magnitude as due to dye, making it important for accurate buoyancy measurements. Furthermore, we show the importance of removing PLIF image stripes and lens vignetting. We apply these techniques to a turbulent round plume, and present results of simultaneous velocity and buoyancy measurements.

Introduction

Understanding turbulent buoyant jets and plumes is central to quantifying the entrainment and mixing processes that occur in a wide range of industrial and natural flows. An accurate prediction of these processes are key for both the optimal design of the discharge facilities and the related environmental impact assessment. Typical laboratory experiments employ salt water and fresh water to obtain the required density differences. However, experimentalists are faced with the challenge of measuring density and velocity field simultaneously to capture the full flow dynamics. Early investigations such as that of Ellison and Turner (1959) took fluid samples to obtain density readings and measured local velocities by adding plastic particles in the flow and photographing it. With the emergence of digital cameras and powerful illumination through laser light, it became possible to access density information in a plane using laser-induced fluorescence (LIF) without the need to place devices within the flow. The use of laser for measurements gave rise to another challenge involved with buoyant flows. The change in density in the flow is accompanied by a change in refractive index. This impairs the accuracy of determination of the particle position in the technique of particle image velocimetry (PIV) for obtaining velocity measurements, and also causes local intensity changes in PLIF. The problem gets more severe in large scale flows where, small variation in refractive index may result in large errors due to large distances laser beam has to travel in the medium. To remove the uncertainties, refractive index matching (RIM) of fluids was first suggested by McDougall [2] for laser doppler velocimetry (LDV) measurements. He investigated several combinations of water solutes, and recommended epsom salt and sugar. Hannoun *et al.* [3] suggested a combination of ethanol and common salt (NaCl) [hereafter called ES]. Here the major advantage is the cost required to obtain same density difference because ethanol reduces the solution density as compared to previous combination where both solutes raise the density. This combination was also suggested by Daviero *et al* (2001) for large scale experiments again owing to the cost. They provided attenuation coefficients for dye, ethanol and salt independently, which have been used in some recent studies involving PLIF measurements [4]. Alahayari and Longmire [1], on the other hand proposed a combination of glycerine and mono-potassium phosphate [hereafter called GP], which offers several advantages over ethanol and salt combination. Although they used chemical chart values of density and refractive index of the solutions, it was shown that a larger density difference of 4% can be achieved with a refractive index variation of 0.0001 compared to only 2% for ethanol-salt combination. For 2% density difference solution ES produces viscosity difference of roughly 60% compared to only 3% for GP. Ethanol increases the temperature of the solution and is highly flammable, also it is found in the present study that glycerine causes approximately half the attenuation caused by ethanol. Furthermore, the cost of GP solution is comparable to ES solution. Owing to all these reasons, GP combination is chosen for the present study.
In the following sections, we will present a description of current experimental set-up for simultaneous measurement of time-resolved velocity and density fields through a combined PIV and PLIF approach. Then, we will discuss the general concept of the PLIF technique, and thereafter we treat the specific issues of the implementation. Finally, we will present the results, especially of turbulent buoyancy flux, which can only be obtained by simultaneous density and velocity measurements.

Experiments

A schematic of the experimental set-up is shown in figure 1. The experiments are conducted in a glass test tank (1.2m high and 0.75m long and wide) filled with a solution of water and mono-potassium phosphate to a depth of 1m. The side-walls are made of 15mm thick clear glass, and bottom wall constructed from marine grade aluminium is removable, allowing us to change the inlet conditions. A buoyant jet of water and glycerine solution is driven by a constant-head tank and discharged from a 3D printed nozzle with exit diameter of 1cm. Three PCO-dimax HS4 12 bit high speed cameras with 32 GB of RAM were used for the measurements. As PIV provides lower resolution compared to PLIF, two cameras were stacked over each other for PIV, and one was placed on the opposite side of the tank for PLIF. PIV cameras are attached with 105mm lens and 532nm bandpass filters with half width of 10nm, whereas PLIF camera is fitted with 60mm lens and 550nm bandpass filter with

half width of 25nm. The filters keep the frequencies of scattered laser light and dye fluorescence out of, respectively the PLIF and PIV cameras. The field of view of PLIF camera is 12cm×12cm and that for PIV cameras is 6.5cm×6.5cm with a overlap of 1cm. All three cameras are synchronized and operate at a frequency of 1000Hz with a resolution of 2000×2000 pixels. Flow is illuminated by Spectra Physics EV25 diode pumped solid state continuous laser. The laser can produce maximum power of 25W at 532nm but it is operated at 10W for all the present experiments.

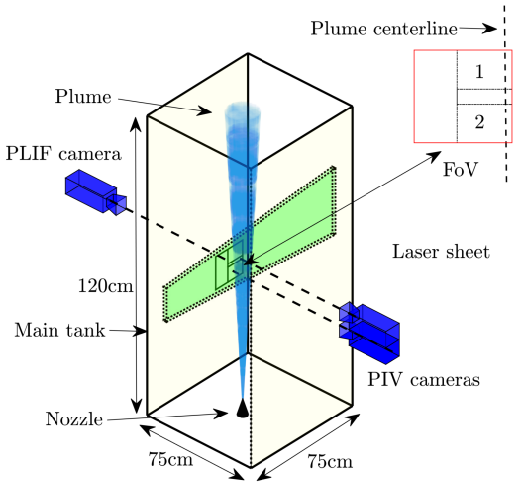

Figure 1: Experimental setup schematic. Exaggerated field of view is shown on the top right. The red box represents the PLIF field of view and boxes numbered 1 and 2 represent the PIV cameras field of view. Dashed line shows the plume centerline.

PLIF theory

Fluorescence is an optical phenomenon in which a chemical compound absorbs photons at a particular wavelength (λ_{abs}) and emits light at a different wavelength (λ_{em}). The general relation between the local fluorescence emitted (F), laser intensity (I) and concentration (C) is:

$$F \propto \frac{I}{1+I/I_{sat}}C, \tag{1}$$

where I_{sat} is the saturation intensity of the dye. In the limit $I \ll I_{sat}$, known as 'weak excitation', (1) can be linearised to,

$$F \propto IC. \tag{2}$$

Equation (2), gives a direct way to estimate concentration by measurement of fluorescence by a camera and a known laser intensity. However, typically the local intensity is unknown and is not measured independently. It can also vary spatially and temporally based on the instantaneous concentration. As the laser sheet passes through a medium, the intensity decreases along the laser beam path, expressed mathematically by Beer-Lambert law,

$$I(r) = I(r_0)\exp\left(-\int_{r_0}^{r}\varepsilon C(s)ds\right), \tag{3}$$

where r_0 is the virtual radial origin from where the laser enters the medium. Using (2) and (3), the fluorescent intensity along the optical path can be expressed as

$$F(r) \propto I(r_0)\exp\left(-\int_{r_0}^{r}\varepsilon C(s)ds\right)C(r), \tag{4}$$

where the integration is for a fixed θ and along a specific r (see figure 2). The imaged fluorescence intensity (F_{cam}) at any pixel is then given by

$$F_{cam}(i,j) = \alpha(i,j)I(r_0)\exp(-\beta(r;\theta))C(r;\theta), \tag{5}$$

where (i,j) are the Cartesian pixel location or the corresponding location in physical space where F_{cam} is measured; $\alpha(i,j)$ is the proportionality constant obtained by calibration procedure explained in the next section; and β includes extinction contribution due to water, dye, salt, glycerine and seeding particles present in the medium.

$$\beta(r,t) = \int_{r_0}^{r}(\beta_w+\varepsilon_d C_d(s,t)+\varepsilon_s C_s(s,t)+\varepsilon_g C_g(s,t)+\varepsilon_{seed}C_{seed})ds, \tag{6}$$

where integration is for a fixed θ. The next section explains the calculation of β from all its contributors as shown in (6). Note that once α, β, $I(r_0)$ and F_{cam} are known, (5) can be used to find C. However, F obtained from the camera can not be used directly, but it has to be 'cleaned' before employing (5), and this will also be clarified in coming section.

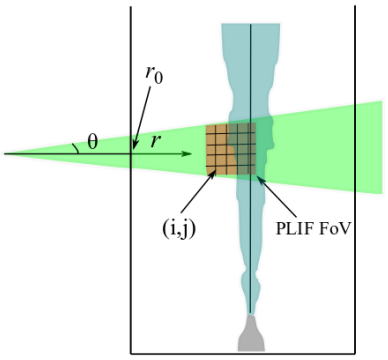

Figure 2: Front view of the setup. r and θ show the direction of integration in equation 3 and 6.

Extinction coefficient

Dye, salt and glycerine

Rhodamine 6G is selected for the present experiments as the peak excitation wavelength (525nm) of the dye is close to the wavelength of the available laser (532nm). Equation (5) can be used to calculate extinction coefficient for any water solute by keeping the concentration constant and knowing the distance that the laser sheet travels in the medium. Attenuation coefficients for dye, glycerine and salt are calculated independently. The procedure is explained for dye, and the same is used for all the solutes. The tank is filled with water to a depth of 20cm to reduce the quantity of solute required, and a known amount of dye is added to the tank in steps of 15μg/L till 150μg/L. 1000 images for each concentration are captured. Figure 3a shows a raw image (F_{img}) obtained at uniform (60μg/L) of dye. It can be clearly observed that the image is hampered by the formation of stripes like pattern (common in PLIF literature) and camera lens vignetting. The maximum intensity in the image is in the middle instead of the left, where the laser sheet enters the field of view. The raw image also includes noise from the camera sensor, which is removed by subtracting dark response (F_d) of the camera, obtained by capturing images with the lens cap on. All of these have to be accounted for an accurate estimation of extinction coefficients.

Stripes in the images are corrected using the filter algorithm provided by Munch *et al.* [5]. The filter uses combined wavelet and Fourier transform approach that allows for isolating and removing the stripe effect without affecting the rest of the image. In Fourier domain, all structural information of a signal is entirely represented by frequencies, whereas any spatial information is distributed over the entire frequency range and thus hidden. In contrast, for the wavelet transform, signal is broken into narrow groups of wavelets of different sizes and frequencies and both,

spatial and frequency information is retained. In the first step, the original image is wavelet decomposed in order to separate the structural information into horizontal, vertical and diagonal details band at different resolution scales. Then, bands containing the stripe information (step change in intensity running along the whole image) are FFT transformed to further tighten the stripes into narrow bands. The condensed stripe information is then eliminated by multiplying it with a Gaussian damping function. Finally, the de-striped image is reconstructed from the filtered coefficients. Here we symbolically use an operator $O_{stripes}$ to denote the stripe removal from an image.

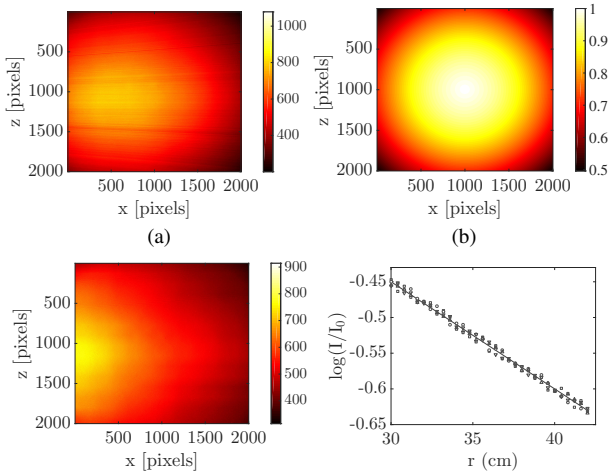

Figure 3: (a) Raw image (F_{img}) at 60μg/L . (b) Estimated vignetting. (c) F_{cam} obtained after background subtraction, stripes removal and vignetting correction. (d) Exponential fit based on (5) at two different concentrations (30μg/L and 60μg/L) and two randomly chosen paths along the laser sheet.

After removing the stripes, the image is corrected for vignetting (to be shown with a symbol O_{vign}). This correction is implemented with an algorithm proposed by Zheng *et al.*[6]. The algorithm uses physical property of vignetting of radial continuous variation of intensity, to distinguish between vignetting and other sources of intensity variations. The images are first broken down into coarse segments and examined for radial intensity variation. This step is repeated by making the segments finer, and finding a global variation estimate by comparing the segments at all scales. Figure 3b shows estimated vignetting for the given raw PLIF image; this is then used to normalize the intensity values in raw image and correct for vignetting. Symbolically the image is processed as:

$$F_{cam} = O_{vign}[O_{stripes}[F_{img} - F_d]]. \tag{7}$$

Figure 3c shows the final corrected camera image (F_{cam}) after applying (7), and it can be seen that the brightest region now corresponds to the entry of laser sheet as expected.
Although stripes cause issues in accurate measurement of intensity, they inadvertently help in finding out the apparent angle subtended by the laser sheet. The stripes can be extended backwards to the sheet origin, and hence find r_0 in (3). This allows integration along the light path, which results in a more accurate estimation of attenuation of the intensity along its path. We note that, for simplicity in most other studies the integration is performed along horizontal (or vertical) directions.
At uniform dye concentration (5) reduces to $F_{cam} = \alpha I(r_0)\exp[-\varepsilon_d C_d (r - r_0)]$. So, to obtain extinction coefficient for dye, the ratio of $F_{cam}(r)/F_{cam}(r_0)$ is taken along the same radial direction. With known values of F_{cam}, C_d and distance travelled in the medium $(r - r_0)$, the only unknowns remaining in the equation are ε_d and α. On an average, variations in α, over the whole range concentrations of dye at every pixel is very small (see figure 6a). Therefore, treating the average α as a constant, the equation can be directly solved for ε_d. Figure 3d shows an exponential fit for two different concentrations of dye (30μg/L and 60μg/L). Extinction coefficient (in units of cm^{-1}(μg/L)$^{-1}$) obtained for the dye ($\varepsilon_d = 0.00025$) matches well with the available value of 0.00023 obtained by Daviero *et al.* [7]. After following the same procedure, extinction coefficients for MPP and glycerine are obtained for the first time. Figure 4a shows the linear fits between εC and C for all three water solutes. The fits are extended to zero concentration of each solute to find attenuation due to water. For MPP, the value ($\varepsilon_s = 0.00011$) is slightly less than that of NaCl ($\varepsilon_{NaCl} = 0.000124$). However, for glycerine it ($\varepsilon_g = 0.00032$) is approximately 40% lower than that of ethanol ($\varepsilon_e = 0.000547$ [7]).

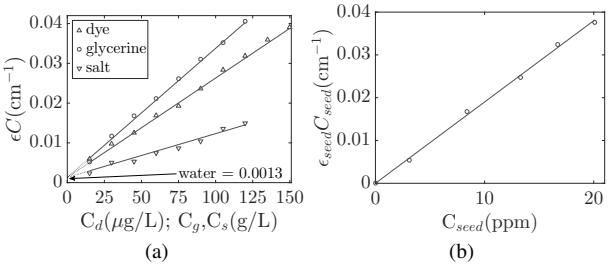

Figure 4: (a) Extinction coefficient for dye, glycerine and mono-potassium phosphate. (b) Extinction coefficient for seeding particles.

Seeding particles

Even though combination of flow seeding and LIF is common in the literature, attenuation caused by the PIV seeding particles has seldom been considered. Cowen et al [8], established a linear relationship between the extinction coefficient and seeding density given as a mass fraction. Same relation was adopted by Krug *et al.* [4] in there combined PTV-LIF study. Both of these studies involve PTV for velocity measurement, where seeding densities are lower compared to PIV. Hence, attenuation due to seeding particles should be significantly higher in combined PIV-LIF studies (owing to the higher seeding density in PIV) and should be taken into account for accurate concentration estimate. Estimating attenuation due to particles requires counting the number of particles in the field of view. In PTV, this is easy as each particle is tracked for velocity hence number of particles are known. In PIV it has to estimated independently. Hence, the tank is filled with a known dye solution already quantified in the previous section, and seeding density C_{seed} is gradually changed. Here we define:

$$C_{seed} = 10^6 \frac{\rho_p \frac{4}{3}\pi {r_p}^3 n_p}{\rho_w V_w}. \tag{8}$$

in parts per million (ppm), where ρ_p, r_p and n_p are particle density, radius and number, and ρ_w and V_w are the water density and volume. Hollow glass spheres of density ρ_p = 1.1g/L and radius r_p = 5μm are used. To estimate the number of particles in a PIV image, it was first converted to a binary image. 'Regionprops' function in Matlab is used to find the locations of each bright blob in the image to calculate its centroid. Number of centroids obtained then represents the number of particles. Figure 5a shows a typical PIV image with a zoomed in view in the inset, and figure 5b is the PDF of number of particles estimated over the thousand images at one seeding density (C_{seed} = 9.5ppm). The extinction coefficient obtained is 0.0019 (see

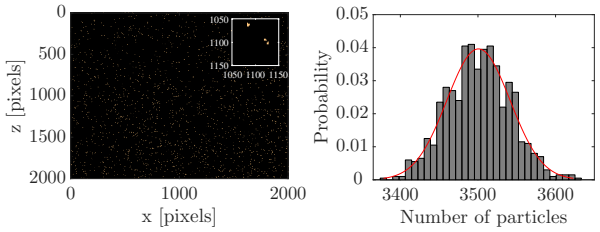

(a) (b)

Figure 5: (a) Raw PIV image with zoomed in portion in the inset. (b) PDF of number of particles from 1000 images captured at one seeding concentration (9.5ppm).

figure 4b), which is very close to 0.002 obtained by Cowen *et al* [8].

Calibration

After calculating β and all its contributors, the next unknown in (5) is α. Here, α accounts for all the contributions from the optical set-up i.e, laser sheet intensity variation in the direction normal to laser path, pixel to pixel bias in camera sensor etc. For this purpose, images are recorded with different known homogeneous concentrations of the dye, C_d, present in the tank. A linear fit to the intensity values averaged over 1000 images is obtained at every pixel at each concentration. Figure 6a shows the fits at 4 randomly picked locations in the image.

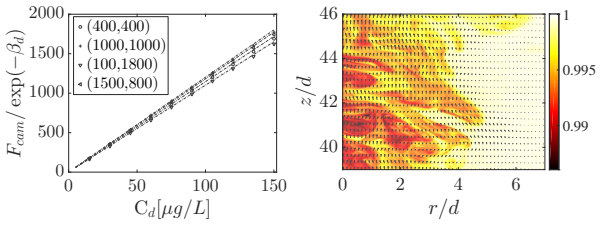

(a) (b)

Figure 6: (a) Linear fit between intensity and concentration at four randomly chosen pixel locations. (b) Instantaneous density normalized by ambient density in background, superimposed with velocity vectors (every fourth vector is shown for clarity). r and z are the radial and streamwise distance, and d is plume nozzle diameter.

PLIF implementation

Using (5), (6) and (7), the instantaneous concentration at any time instant t can be written as,

$$C(i,j;t) = \frac{F_{cam}(i,j)}{\alpha(i,j)\,I(r_0)\,\exp(-\beta(i,j;t))}. \qquad (9)$$

To obtain the local dye concentration from the LIF images, the following procedure is used. First, a median filter is applied to the images to effectively remove very small contributions from light scattered by particles that passed the bandpass filter. The size of the filter kernel is 5×5 pixels, which proved large enough to remove all spurious particle images. Next, the pixel intensity is converted to concentration using (9). $\alpha I(r_0)$ is obtained in the calibration process and is same for all the time instants. β at t = 0 is calculated using (6) for known concentration of salt in the tank. Once the concentration of dye is obtained at t = 0, it is used to calculate concentration of glycerine, and β is updated to be used for the image at the next time instance.

Results

Figure 6b shows the instantaneous velocity and density in the plume for the nozzle exit Reynolds number of 2600 and Richardson number of 0.23, from z/d = 39 to 46. Figure 7a shows the velocity and buoyancy profiles at different z locations. Both profiles are Gaussian and the buoyancy width is slightly wider than the velocity width. The ratio of the widths (buoyancy/velocity) is 1.05, agreeing to the value, 1.04 obtained by Wang and Law [9]. Figure 7b shows the axial buoyancy flux matching well with the available data [9].

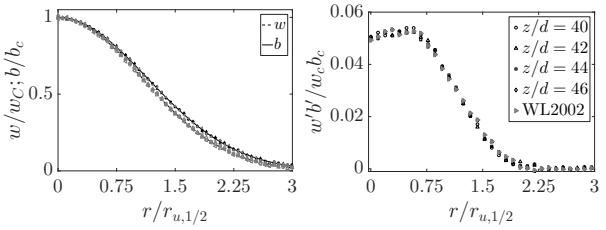

(a) (b)

Figure 7: (a) Axial velocity (w) and buoyancy (b) profiles at different z locations normalized by the centerline values. (b) Normalized axial turbulent buoyancy flux overlaid with data from WL2002 [9]. $b = g(\rho_a - \rho)/\rho_a$ and and $r_{u,1/2}$ is the radial distance, where the magnitude of streamwise centerline velocity reduces to half.

Conclusions

Simultaneous measurements of velocity and density in a turbulent buoyant plume is carried out using PIV and PLIF. Attenuation coefficients for refractive index matching combination of glycerine and mono-potassium phosphate are obtained for the first time. This combination, apart from being safer to use, causes less attenuation of laser sheet, and hence can be used for larger density differences as well as large scale experiments. Attenuation due to particles, which till date was only considered in few PTV studies is obtained and confirmed. It is observed that this can not be ignored, especially with high seeding density of PIV, with the attenuation being of same order of magnitude as for the dye. The first and second order statistics in plume satisfactorily match the data from literature. Now the data can be used for further investigation like, calculation of profile coefficients of momentum, buoyancy and turbulence production, which are ignored in the standard classical models for plumes.

Acknowledgements

The authors gratefully acknowledge the Australian Research Council for the financial support of this work.

References

[1] A Alahyari and E.K Longmire. *Exp. fluids*, 17(6):434–440, 1994.

[2] T.J Mcdougall. *J. Fluid Mech.*, 94(3):409–431, 1979.

[3] I.A Hannoun, H.J.S Fernando, and E.J List. *J. Fluid Mech.*, 189:189–209, 1988.

[4] D Krug, M Holzner, B Lüthi, M Wolf, A Tsinober, and W Kinzelbach. *Meas. Sci. Technol.*, 25(6):065301, 2014.

[5] B Münch, P Trtik, F Marone, and M Stampanoni. *Optics express*, 17(10):8567–8591, 2009.

[6] Y Zheng, S Lin, C Kambhamettu, Jingyi Y, and S. B Kang. *IEEE Trans. Pattern Anal. Mach. Intell.*, 31(12):2243–2256, 2009.

[7] G.J Daviero, P.J.W Roberts, and K Maile. *Exp. fluids*, 31(2):119–126, 2001.

[8] E.A Cowen, K.A Chang, and Q Liao. *Exp.fluids*, 31(1):63–73, 2001.

[9] H Wang and A.W Law. *J. Fluid Mech.*, 459:397–428, 2002.